JOURNAL OF THERMOPHYSICS AND HEAT TRANSFER
Vol. 17, No. 1, January–March 2003

Melting in Microgravity

M. E. Glicksman* and A. Lupulescu†
Rensselaer Polytechnic Institute, Troy, New York 12180-3590
and
M. B. Koss‡
College of the Holy Cross, Worcester, Massachusetts 01610-2395

The Isothermal Dendritic Growth Experiment constituted a series of three NASA-supported microgravity experiments (USMP-2, -3, and -4), which flew aboard the space shuttle *Columbia*. These space flight experiments grew and recorded dendrites in the absence of gravity-induced convective heat transfer. USMP-4, for the first time, allowed streaming of near-real-time video data. Using 30-fps video data, we studied both freezing and melting sequences for pivalic acid (PVA) at different supercoolings. We report on the melting process of a PVA dendritic mushy zone, observed for the first time under convection-free conditions. Conduction-limited melting processes are of importance in orbital melting of materials, meteoritic genesis, mushy-zone evolution, and in fusion weld pools where the length scales for thermal buoyancy are highly restricted. Microgravity video data show that PVA dendrites melt into fragments that shrink at accelerating rates to extinction. The melting paths of individual fragments follow a characteristic time dependence for the diminishing length scales within the mushy zone. The theoretical melting kinetics against which the experimental observations are compared is based on the conduction-limited quasi-static process of melting under shape-preserving conditions. Good agreement between theory and experiment was found for the melting of a selected needle-shaped prolate spheroidal PVA crystal fragment with an aspect ratio of $\mathcal{C}/\mathcal{A} = 12$.

I. Introduction

A. Dendritic growth: Background

DENDRITES (tree-like crystals) represent highly evolved microstructures arising from unstable solid–melt interfaces.[1] In fact, dendrites are the ubiquitous form of crystal growth encountered whenever metals and alloys solidify freely from supercooled melts or solidify directionally under low thermal gradients. These highly branched solidification structures are responsible for the microsegregation of solutes, which is often associated with the formation of defects that occur in castings and ingots. The speeds and length scales of dendritic crystals reflect the solidification conditions, including temperature, composition, and supersaturation of the melt. Dendrite development itself is important because it influences the properties and responses of cast materials, for example, texture, strength, plasticity, and corrosion resistance.

Many theoretical[2–5] and experimental[6–9] dendritic growth studies have been reported over the past half-century. Today, in fact, we view dendritic growth as resulting from the coupling of two processes: 1) the steady-state diffusion-limited advance of the dendrite tip and 2) the capillary-mediated wave-like evolution of dendrite branches. Dendrite growth is much simpler to describe in the case of free growth from a pure molten phase. The thermodynamic driving force for crystallization in this case is the melt supercooling $\Delta T \equiv T_m - T_\infty$, where T_m is the melting point of the material and T_∞ is the temperature of the melt far from the heat emitting solid–liquid interface. The crystallization process for free growth requires that the latent heat released be transported away from the solid–liquid interface by thermal transport to the cooler (supercooled) melt. In the more complicated case of alloys—not treated any further here—the thermodynamic driving force for dendritic growth is the melt supersaturation. In alloys, one must consider both the thermal and solutal boundary layers associated with the simultaneous transport of latent heat and solute atoms.[10]

Specifically, we analyzed and report the first on-orbit video data that record carefully controlled growth and melting sequences in convection-free dendritic mushy zones obtained under microgravity conditions. This paper provides an analysis of melting sequences of already formed dendrites in microgravity—a subject not developed in much detail in the prior literature.

B. Isothermal Dendritic Growth Experiment (IDGE)

Mathematical analysis of the dendritic growth problem in pure substances consists of two parts: 1) solving the energy equation along with appropriate boundary conditions for the temperature field at the moving solidification front and 2) accounting for capillary effects introduced at the curved dendritic interface, including the morphological stability of the solid–liquid interface. Basic theories of dendritic growth in pure materials are best tested under heat conduction controlled conditions, where the gravitational acceleration is, in principle, reduced to zero, and convective heat transport in the molten phase is eliminated.[11–14] IDGE is a basic science experiment designed to provide terrestrial and microgravity data that measure the kinetics and morphology of dendritic solidification under pure heat conduction control. Before the advent of IDGE in 1994, it was not possible to test quantitatively either Ivantsov's transport solution[15] for the steady-state thermal field surrounding a steady-state dendrite, or evaluate the so-called interfacial "stability constant" $\sigma^* \approx 0.02$, as predicted from various physics theories of the solid-liquid dendritic interface.[2–5] The IDGE flew three times as a primary payload on the USMP-2, -3, and -4 missions, in 1994, 1996, and 1997, respectively, aboard the space shuttle *Columbia*. These flight experiments provided the first solid evidence that Ivantsov's heat-conduction solution closely describes dendritic growth for the test materials succinonitrile and pivalic acid (PVA). These organic crystals offer three major experimental advantages compared to metals: they are transparent, easily purified to high levels, and have conveniently low melting points. The onboard IDGE instruments provided charge-coupled device images (telemetered to Earth during the flights), NASA-processed 35-mm film negatives

Received 23 January 2002; revision received 17 June 2002; accepted for publication 10 September 2002.

*Professor, Materials Science and Engineering Department.
†Research Assistant Professor, Materials Science and Engineering Department.
‡Professor, Department of Physics.

(available postflight), and for the first time on USMP-4 near-real-time streaming of video data telemetered to our laboratory via the K-band (high-frequency) antenna on the shuttle. IDGE data in its totality, as reported elsewhere, consisted of hundreds of repeated experiments on steady-state dendritic growth. These data provide benchmark quality crystal growth speed as well as tip radii measured as functions of the melt supercooling, ΔT.

C. Mushy Zones

Dendrites are the key microstructural components of mushy zones. A mushy zone is defined as a finely mixed two-phase region, consisting of a dendritic primary solid phase embedded within its melt phase. Mushy zones are known to be present in ingots, castings, and welds, and are thought to play a role in the evolution of the Earth's core and planetesimals. The mushy zone represents the "active" region in a solidifying body in which the microstructure forms and evolves. The dendritic structures that form in mushy zones are often highly ramified, as a result of the growth of multiple primary dendrites and the subsequent development of secondary, tertiary, and even higher-order side branches. Consequently the length scales for melt convection within mushy zones are usually small, micron-sized pockets of melt remaining between dendrite arms. Under terrestrial conditions, to characterize a mushy zone one must understand a number of complex processes. These include conduction and convection of latent heat, solid-state diffusion of solute segregated among the dendritic branches, limited convective transport of solute in the melt, and capillary effects such as remelting and phase coarsening.[16,17] To simplify the behavior of a melting mushy zone, we studied pure PVA (4-9's purity) under nearly gravity-free conditions. In a carefully controlled microgravity environment ($g \leq 10^{-6} g_0$, where g_0 has the terrestrial value of 9.8 m/s^2) the melting of a mushy zone in a pure substance should be kinetically controlled by a conduction-limited heat-transfer process, perhaps slightly modified by capillarity.

Thermodynamically, a melting process is a first-order phase transition (solid-to-liquid), where the melting coexistence curve defines a temperature-pressure relation for which the chemical potentials of the components remain equal in the solid and melt. The entropy of melting is almost always positive, the volume change on melting is usually small and positive, and the melting point therefore normally increases as pressure increases. The kinetics of melting, however, has previously been studied in the presence of relatively strong buoyancy-induced melt convection. Convection alters the thermal fields surrounding dendrites, and strong gravitational sedimentation also takes place because the solid and melt usually differ by a few percent in their mass densities. Conduction-limited freezing and melting processes in microgravity are of importance in both terrestrial and planetary processes. For example, mushy-zone evolution in castings and ingots, fusion welding, Earth's core processes,[18–23] meteoritic and planetary genesis[24–26] all occur either where gravity is absent, or where the mushy zone length scales for thermal buoyancy are highly restricted and little convection occurs.

II. Analysis of IDGE Video Data

The freezing and melting data analyzed and reported here are near-real-time 30-fps video downlinked from the third and final IDGE microgravity experiments. The IDGE video database represents an unique compilation of scientific information concerning the kinetics of freezing/melting of PVA (face cubic centered) dendritic crystals. Onboard video signals generated within the IDGE were downlinked via the shuttle's K-band antenna and recorded by NASA on 8-mm tapes using a high-resolution VTR. The analog data were transferred via coaxial cable to an image capture card using commercial software (VideoSavant©). Two hours of 30-fps, 640 × 480, 255 grayscale images are captured on a single, large-image buffer file, accessed by VideoSavant. The image processor/compiler required approximately 70 GB of hard drive memory. Once the image buffer is viewed by software, we could export the digitized video at the desired rate in the following file types: .avi files for illustration, .tiff files, or .jpeg files for analysis.

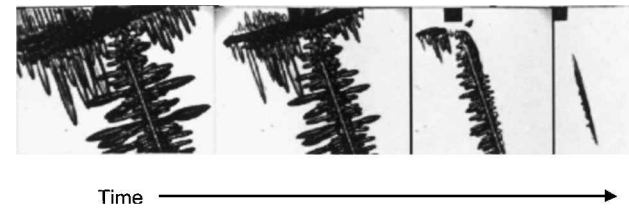

Fig. 1 Video frames showing the progressive melting of a PVA dendritic mushy zone in microgravity. As the dendrites fragment, the individual crystallites remain motionless in the melt. Video data analyzed for the terminal melting of the needle crystal shown in the last panel.

Each IDGE experimental cycle consisted of the following five stages, repeated over and over as the space flight continued on orbit:

1) Begin with the PVA melt in a thermodynamically stable, isothermal environment, with $T \geq T_m$.

2) Reduce the thermostat temperature to cool the melt and establish to within ± 0.002 K isothermal conditions at a predetermined supercooling so that $T \leq T_m$.

3) Nucleate the growth of dendrites by activating a thermoelectric cooler to chill a small isolated volume of the melt sufficiently to initiate crystal growth.

4) Photograph the emergence and steady-state crystal growth of dendrites with still and 30-fps video cameras and form the mushy zone, causing latent heat release and $T \rightarrow T_m$.

5) Raise the thermostat temperature to remelt the dendritic mushy zone, thereby returning the system to a stable melt phase $T \approx T_m + 1.8$ K.

For each freezing/melting cycle, the video data (steps 4 and 5) were exported as individual .tiff files for every tenth frame. For the last minute of melting, toward the end of step 5, where the thermal fields approach the stable melt temperature, approximately 1.8 K above T_m, individual .tiff files were exported for every video frame.

As melting begins, the tertiary dendritic side-arms begin to shorten, and the larger secondary branches detach from the primary stem. Figure 1 shows several stages of the melting sequence. In microgravity the individual crystalline elements of the mushy zone remain completely motionless. We did not observe any sedimentation of the fragments of denser solid. At the final stages the remaining dendritic fragments present a large variety of shapes, from nearly spherical blobs to elongated needle-like crystals, all of which eventually melt away.

The mushy-zone melting events recorded every 1/30th s as digital frames provides, to our knowledge, the first data compilation of convection-free melting over a significant range of length scales, from about 10^{-2} m down to about 5×10^{-5} m. The large dynamic range of these length scales allows a detailed kinetic analysis of the convection-free melting process.

III. Data Analysis—Image Processing

The shapes of the melting dendritic fragments, as analyzed from the IDGE video data, were determined using commercial image analysis software (ImagePro© 4.0). The fragments, particularly toward the later stages of melting, are best described as prolate spheroidal particles. Figure 2 shows the shape of a melting dendrite stem outlined using this software tool. The equivalent ellipse of the two-dimensional image of this fragment is calculated on the basis of its major axis $\mathcal{C}$ and minor axis $\mathcal{A}$. The physical particles are, of course, three-dimensional objects, approximated as prolate spheroids of decreasing size. A prolate spheroid is an ellipsoid where the two minor axes are equal. Image analysis permitted measurement of the major and minor axes of the equivalent ellipsoidal fragment as a function of time. Sampling the $\mathcal{C}/\mathcal{A}$ ratio over time towards the end of the melting cycle shows that the values of the $\mathcal{C}/\mathcal{A}$ ratio for a particular fragment do not vary much. Figure 3 shows how the $\mathcal{C}/\mathcal{A}$ ratio changes with time. For the particular crystal measured, the $\mathcal{C}/\mathcal{A}$ ratio varies from a starting value of about 11, rises to a maximum of about 14, and decreases to a value of 10 with about 95% of the crystal's volume melted. Thus, the $\mathcal{C}/\mathcal{A}$ ratio for

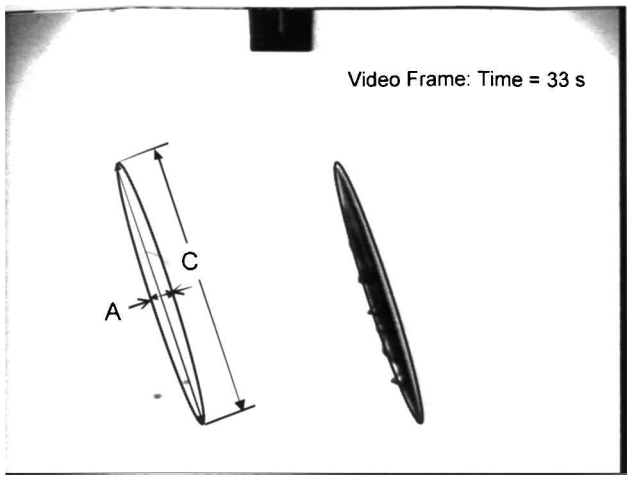

Fig. 2 Sample digitized video frame used for image analysis of a melting dendritic fragment. The image analyzer provides the equivalent ellipse for the fragment, allowing determination of its major axis length $\mathcal{C}(t)$ and its $\mathcal{C}/\mathcal{A}$ ratio.

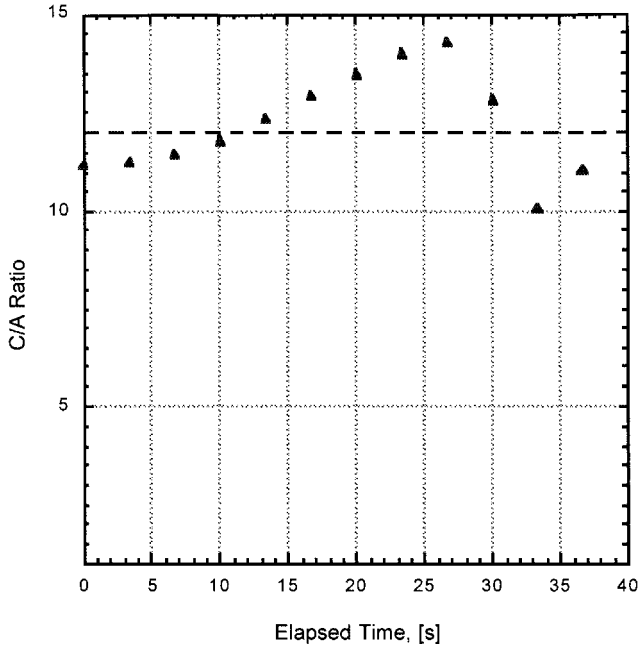

Fig. 3 Aspect ratio of the melting crystal fragment vs time. Data derived by image analysis of video frames of a dendritic PVA fragment melting in microgravity. The volume-weighted average of the aspect ratio for this crystal is $\mathcal{C}/\mathcal{A}$ = 12.

the melting fragment can be approximated by its volume-weighted average, which in this instance is $\langle \mathcal{C}/\mathcal{A} \rangle = 12.0$.

Quasi-static and moving boundary solutions are well known for the growth of spherical crystals for which $\mathcal{C}/\mathcal{A} = 1$ (Refs. 27 and 28). For the more general cases of ellipsoids and hyperboloids, moving boundary solutions were developed by Ham.[29] Moving boundary solutions for elliptical paraboloids and parabolic cylinders were developed by Horvay and Cahn.[30] However, Ham's similarity solutions for ellipsoids apply only to the case of crystal growth, for which, curiously, they represent morphologically unstable mathematical solutions[31] (see also, Sekerka, R. F., personal communication, Aug. 2002). Ham clearly states in his paper that the similarity transformations used in his moving boundary solutions are inapplicable to cases of ellipsoidal particle melting. Lacking an analytical moving boundary solution, we developed a quasi-static model for the conduction melting of prolate spheroids, and subsequently demonstrate that the melting kinetics, without convection, of needle-like dendritic fragments is accurately described as a conduction-limited process.

IV. Quasi-Static Theory

A. Potential Theoretic Formulation

The quasi-static melting or freezing of a crystal is based on determining the heat current entering or leaving its static solid–melt interface and then formulating kinematic equations for the crystal's shrinkage or growth. The rate of change of the particle's volume is assumed to occur slowly enough that the surrounding transport field has sufficient time to adjust to the changing particle. The thermal transport field used only approximates the time-dependent solution to the conduction equation as a quasi-static solution based on Laplace's equation. The key condition determining the applicability of such approximations is that the Stefan number [defined in Eq. (2)]—the intensity measure for melting or freezing—is small.

We first choose cylindrical coordinates (r, z, φ) to describe a prolate spheroidal crystal with major axis $\mathcal{C}$ and minor axis $\mathcal{A}$. The crystal's major axis is aligned with the z axis. The plane $z = 0$ is the equatorial plane that divides the crystal symmetrically, so that its poles ($r = 0$) occur at $z = \pm\mathcal{C}/2$. The axis-symmetric temperature field $T(r, z)$ will be nondimensionalized as a potential ϑ defined as

$$\vartheta(r, z) \equiv \frac{T(r, z) - T_m}{T_\infty - T_m} \tag{1}$$

where T_∞ is the temperature of the melt infinitely far away from the particle. The propensity and rate of melting (or freezing) is determined by the sign and magnitude of the denominator in Eq. (1). A convenient dimensionless parameter based on that temperature difference is the Stefan number defined here as

$$St \equiv \frac{T_\infty - T_m}{\Delta H_f \big/ C_\ell^p} \tag{2}$$

where ΔH_f is the molar enthalpy of fusion and C_ℓ^p is the molar specific heat of the melt at constant pressure. It is convenient to express the potential defined in Eq. (1) in an orthogonal, curvilinear coordinate system in which the effect of curvature on T_m is neglected. Consequently, the crystal–melt interface of the prolate spheroid is considered an isothermal coordinate surface labeled $\xi = \Xi$, for which the potential is $\vartheta(\Xi) = 0$. Such a coordinate system (ξ, η, φ) is discussed by Morse and Feshbach,[32] for which the metric coordinates ξ and η are scaled to the interfocal length of the prolate spheroid $a = \mathcal{C}/\Xi = \mathcal{A}/\sqrt{(\Xi^2 - 1)}$. These prolate spheroidal coordinates are displayed in Fig. 4 as the $\varphi = 0$ projection. In brief, heat flow in three dimensions occurs by conduction through the melt along the hyperboloidal surfaces $\eta = \text{const}$. The isotherms of the resultant temperature field are concentric prolate ellipsoids $\xi \geq \Xi = \text{const}$ surrounding a crystal–melt interface $\xi = \Xi$ that remains at the equilibrium melting point.

Specifically, one can easily show that the Laplacian potential surrounding a prolate spheroid with the fixed interfacial potential $\vartheta(\Xi) = 0$, embedded in a melt where the far-field potential $\vartheta(\infty) = 1$, can be expressed in these curvilinear coordinates as

$$\vartheta(\xi, \eta) = 1 - \frac{\log[(\xi + 1)/(\xi - 1)]}{\log[(\Xi + 1)/(\Xi - 1)]} \tag{3}$$

The gradient field associated with the thermal potential given in Eq. (3) is easily found by taking the partial derivative of the potential Eq. (3), $\vartheta(\xi, \eta)$, with respect to ξ, and then dividing the result by the ξ-coordinate scale factor $h_\xi = (a/2)\sqrt{[(\xi^2 - \eta^2)/(\xi^2 - 1)]}$. Carrying out these mathematical operations yields the desired gradient field at all points surrounding a prolate spheroidal crystal, namely,

$$\frac{1}{h_\xi}\frac{\partial \vartheta(\xi, \eta)}{\partial \xi} = \nabla \vartheta(\xi, \eta)$$

$$= \frac{2}{a}\sqrt{\frac{\xi^2 - 1}{\xi^2 - \eta^2}}\,\frac{2}{(\xi + 1)(\xi - 1)}\left(\log\frac{\Xi + 1}{\Xi - 1}\right)^{-1} \tag{4}$$

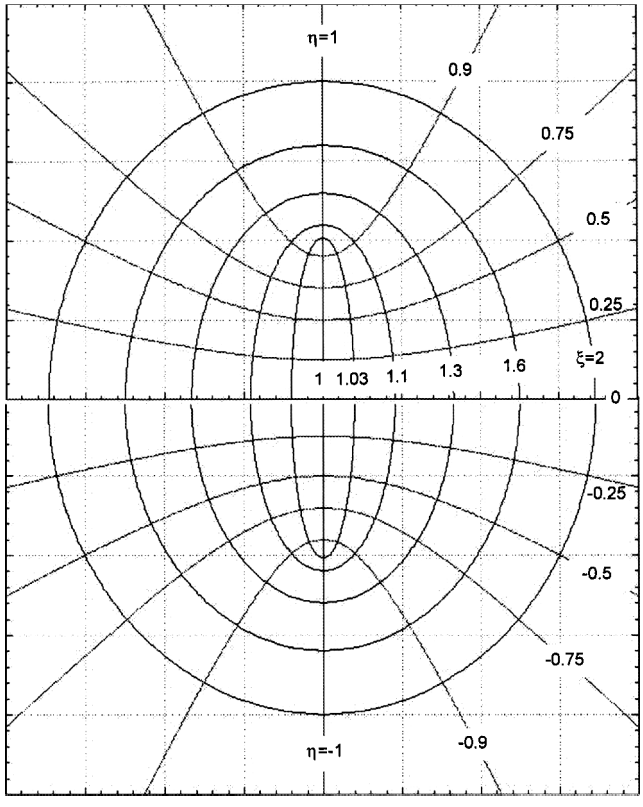

Fig. 4 Prolate spheroidal coordinates (ξ, η, φ) on the $\varphi = 0$ plane. The solid–melt interface has the profile $\xi = \Xi$, where its aspect ratio $\mathcal{C}/\mathcal{A} = \Xi/\sqrt{(\Xi^2 - 1)}$. The isotherms surrounding this crystal are surfaces of the form $\xi \geq \Xi$ = const, and the heat flow follows surfaces of the form η = const.

which can be simplified to

$$\nabla\vartheta(\xi, \eta) = (4/a)\left\{\sqrt{(\xi^2 - 1)(\xi^2 - \eta^2)}\,\log[(\Xi + 1)/(\Xi - 1)]\right\}^{-1} \tag{5}$$

The relationship of the gradient field, Eq. (5), to the actual thermal gradient in the melt can be found by differentiating Eq. (1) with respect to ξ and again dividing through by the curvilinear coordinate scale factor h_ξ,

$$\nabla\vartheta(r, z) = \frac{1}{h_\xi}\frac{\partial T(r, z)}{\partial \xi}\left(\frac{1}{T_\infty - T_m}\right) \tag{6}$$

Rescaling the potential gradient through the characteristic temperature of the material $\Delta H_f/C_\ell^p$ and substituting the definition of the coordinate scale factor h_ξ yields the thermal gradient in the melt at any arbitrary point ξ, η, φ.

$$\frac{\Delta H_f}{C_\ell^p}\nabla\vartheta(\xi, \eta) = \frac{\Delta H_f}{C_\ell^p}\cdot\frac{2}{a}\sqrt{\frac{\xi^2 - 1}{\xi^2 - \eta^2}}\cdot\frac{\partial T(r, z)}{\partial \xi}\left(\frac{1}{T_\infty - T_m}\right) \tag{7}$$

If the temperature gradients are evaluated at the solid–melt interface $\xi = \Xi$, then Eq. (7) can be written in the compact form

$$\left(\Delta H_f/C_\ell^p\right)\nabla\vartheta(\Xi, \eta) = (1/St)\nabla T_\Xi \tag{8}$$

where the definition of the Stefan number, Eq. (2), has been substituted into Eq. (7) and the symbol ∇T_Ξ denotes the dimensional thermal gradient in the melt evaluated at the crystal–melt interface.

B. Enthalpy Current

The enthalpy flux $\boldsymbol{J}$ for thermal conduction through the melt normal to the crystal-melt interface can be found using Fourier's law $\boldsymbol{J} = -k_\ell\nabla T_\Xi$, where k_ℓ is the thermal conductivity of the melt. The gradient at the solid-melt interface, Eq. (8), can be substituted into Fourier's law to yield the thermal flux

$$\boldsymbol{J} = -k_\ell\left(\Delta H_f/C_\ell^p\right)St\cdot\nabla\vartheta(\Xi, \eta) \tag{9}$$

Inserting the expression for the potential gradient, Eq. (5), evaluated on the crystal-melt interface $\xi = \Xi$ into Eq. (9), gives the thermal flux normal to the solid–melt interface as

$$\boldsymbol{J} = -k_\ell\left(\Delta H_f/C_\ell^p\right)St\cdot(4/a)$$
$$\cdot\left\{\sqrt{(\Xi^2 - 1)(\Xi^2 - \eta^2)}\,\log[(\Xi + 1)/(\Xi - 1)]\right\}^{-1} \tag{10}$$

The total energy current entering (or leaving) the "static" prolate spheroid can be expressed as the integral of the flux over its total area $\mathcal{S}$. Thus,

$$\dot{Q}_{\text{tot}} = \oint \boldsymbol{J}\cdot\boldsymbol{n}\,\mathrm{d}\mathcal{S} \tag{11}$$

where the differential element of crystal–melt interfacial area on the prolate spheroid $\xi = \Xi$ can be expressed in the curvilinear coordinates as

$$\mathrm{d}\mathcal{S} = r(\Xi, \eta)\,\mathrm{d}\sigma(\Xi, \eta)\,\mathrm{d}\varphi = r(\Xi, \eta)h_\eta\,\mathrm{d}\eta\,\mathrm{d}\varphi \tag{12}$$

where $r(\Xi, \eta) = a/2\sqrt{[(\Xi^2 - 1)(1 - \eta^2)]}$ is the radial distance from the major axis of the prolate spheroid to an arbitrary point η on the crystal–melt interface; $\mathrm{d}\sigma = h_\eta\,\mathrm{d}\eta$ is the differential of the arc length; and the η-coordinate scale factor needed to relate the arc length σ along the interface expressed in curvilinear prolate spheroidal coordinates is defined by Morse and Feshbach[32] as $h_\eta \equiv a/2\sqrt{[(\Xi^2 - \eta^2)/(1 - \eta^2)]}$. Substituting these transformations into Eq. (12) yields the differential element of interfacial area on a prolate spheroidal crystal:

$$\mathrm{d}\mathcal{S} = (a^2/4)\sqrt{(\Xi^2 - 1)(\Xi^2 - \eta^2)}\,\mathrm{d}\eta\,\mathrm{d}\varphi \tag{13}$$

Substituting Eq. (10) for the normal flux vector and Eq. (13) for the differential interfacial area into Eq. (11) yields the integral expression

$$\dot{Q}_{\text{tot}} = -\frac{ak_\ell\Delta H_f St}{C_\ell^p}\left(\log\frac{\Xi + 1}{\Xi - 1}\right)^{-1}\int_{-1}^{1}\mathrm{d}\eta\int_0^{2\pi}\mathrm{d}\varphi \tag{14}$$

where the integration limits on η ($-1 \leq \eta \leq 1$) and on φ ($0 \leq \varphi \leq 2\pi$) correspond to integrating the total interfacial area from pole to pole on the prolate spheroid $\xi = \Xi$. Carrying out the closed surface integration indicated in Eq. (14) introduces the expected spherical image 4π and yields the total heat current entering a prolate spheroid with an interfocal length a,

$$\dot{Q}_{\text{tot}} = -\frac{4\pi}{\log[(\Xi + 1)/(\Xi - 1)]}\frac{ak_\ell\Delta H_f}{C_\ell^p}St \tag{15}$$

C. Kinematic Energy Balance

Heat entering (or leaving) the prolate spheroidal crystal results in its shrinkage (or growth) caused by the corresponding melting/freezing phase transformation. The time-dependent volume of a melting or freezing prolate spheroidal crystal can be expressed conveniently, applying our notation, in terms of its time-dependent major and minor axes through the formula[33]

$$V(t) = (\pi/6)\mathcal{A}^2(t)\mathcal{C}(t) = (\pi/6)(\mathcal{A}/\mathcal{C})^2\mathcal{C}^3(t) \tag{16}$$

where the time dependence of the spheroid's fixed aspect ratio $\mathcal{C}/\mathcal{A}$ is explicitly suppressed in the right-hand equality. In the case of a sphere of diameter $\mathcal{D}$, the aspect ratio $\mathcal{C}/\mathcal{A} = 1$, $\mathcal{C} = \mathcal{D}$, and the familiar result obtains from Eq. (16).

If the crystalline spheroid melts (or freezes) and is subject to a time rate of change of its volume, then the time rate of change of its major-axis length is related kinematically to the volume derivative as

$$\dot{V}(t) = (\pi/2)(\mathcal{A}/\mathcal{C})^2 C^2(t)\dot{\mathcal{C}}(t) \tag{17}$$

where the overdot notation indicates time differentiation. The rate of enthalpy change associated with the volume change can be expressed as

$$\dot{H}_{\text{tot}} = (\pi/2)(\Delta H_f/\Omega)(\mathcal{A}/\mathcal{C})^2\mathcal{C}^2(t)\dot{\mathcal{C}}(t) \tag{18}$$

where Ω is the molar volume. This enthalpy expression ignores the imperceptible advection occurring in the melt near the interface caused by the small ($\approx$3%) density differences of the phases. Coriell and McFadden have shown that the effect of this advection on the transport of energy to or from the interface, in the case of steady-state dendritic crystallization, is negligible for real materials.[34] Recent work by Karma and Plapp[35] using phase-field computations confirm the findings by Coriell and McFadden.[34]

The kinematic energy balance under quasi-static conditions is therefore $\dot{H}_{\text{tot}} = \dot{Q}_{\text{tot}}$. Equating Eq. (18) with Eq. (15) gives

$$\frac{\pi}{2}\frac{\Delta H_f}{\Omega}\left(\frac{\mathcal{A}}{\mathcal{C}}\right)^2 \mathcal{C}^2(t)\dot{\mathcal{C}}(t) = -\frac{4\pi}{\log[(\Xi+1)/(\Xi-1)]}\frac{ak_\ell \Delta H_f}{C_\ell^p}St \tag{19}$$

Equation (19) provides an O.D.E. describing the quasi-static evolution of a prolate spheroidal crystal of constant aspect ratio and interfocal length a surrounded by an infinite superheated, or supercooled, melt at a Stefan number St. Equation (19) can be solved for the measurable quantity $\mathcal{C}(t)$ by 1) cancelling common terms; 2) recognizing that $k_\ell\Omega/C_\ell^p \equiv \alpha_\ell$, where α_ℓ is the thermal diffusivity of the melt; 3) applying the transformation $a = \mathcal{C}/\Xi$; 4) separating the dummy variables $\mathcal{C}$ and t'; and 5) integrating between appropriate time limits for melting $t' = 0, \mathcal{C} = \mathcal{C}_0$, and $t' = t, \mathcal{C} = \mathcal{C}(t)$.

After applying each of the steps just enumerated, one obtains

$$\int_{\mathcal{C}_0}^{\mathcal{C}(t)} \mathcal{C}\,\mathrm{d}\mathcal{C} = -\frac{8}{\Xi\log[(\Xi+1)/(\Xi-1)]}\left(\frac{\mathcal{C}}{\mathcal{A}}\right)^2 \alpha_\ell St\int_0^t \mathrm{d}t' \tag{20}$$

Carrying out the indicated integrations in Eq. (20) yields, after several steps of algebra, the desired result:

$$\mathcal{C}(t) = \sqrt{\mathcal{C}_0^2 - \frac{16\alpha_\ell St}{\Xi\log[(\Xi+1)/(\Xi-1)]}\left(\frac{\mathcal{C}}{\mathcal{A}}\right)^2 t} \tag{21}$$

Equation (21) can be nondimensionalized as

$$\mathcal{C}(t)/\mathcal{C}_0 = \sqrt{1 - K_{\text{prol}}\cdot St\cdot Fo} \tag{22}$$

where the rate constant is defined as

$$K_{\text{prol}} \equiv \frac{16}{\Xi\log[(\Xi+1)/(\Xi-1)]}\left(\frac{\mathcal{C}}{\mathcal{A}}\right)^2 \tag{23}$$

and the Fourier number (dimensionless time) is defined as

$$Fo \equiv \left(\alpha_\ell/\mathcal{C}_0^2\right)t \tag{24}$$

It is convenient for experimental purposes to be able to relate K_{prol} to the crystal's $\mathcal{C}/\mathcal{A}$ ratio. Equation (23) is cross plotted in Fig. 5 against the function $\mathcal{C}/\mathcal{A} = \Xi/\sqrt{(\Xi^2-1)}$. Aside from questions of its temporal stability, Eq. (21) provides the kinetic law for the growth ($St \le 0$) or melting ($St \ge 0$) of a prolate spheroidal crystal. The morphological stability of melting and freezing prolate spheroids will not be explored in this paper.

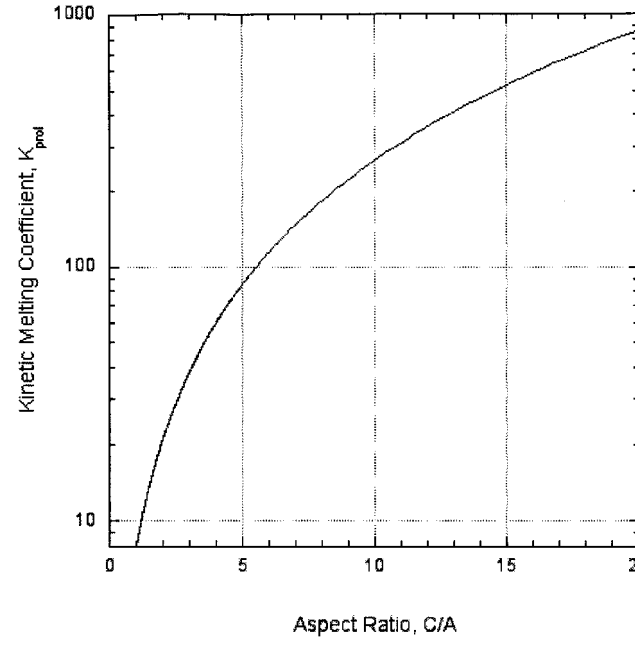

Fig. 5 Quasi-static rate constant K_{prol} vs the aspect ratio $\mathcal{C}/\mathcal{A}$.

V. Results

The crystal analyzed in microgravity formed originally as a part of a dendritic mushy zone in the IDGE growth cycle 4. The dendrites grew from pure molten PVA supercooled 0.4 K. The mushy zone consisted of approximately 4% dendritic solid when melting was initiated. The time to melt this mushy zone completely was approximately 12 min. The last fragment to melt was the one selected for analysis. (See again the last panel of Fig. 1.) This chosen dendrite fragment ($C_0 = 0.76$ cm) was the residual crystal from the melting primary dendrite stem and exhibited a nearly constant aspect ratio $\mathcal{C}/\mathcal{A} \cong 12$ throughout its final 40-s melting sequence. To calculate the melting kinetics of this dendritic fragment, one must know, in addition to the $\mathcal{C}/\mathcal{A}$ ratio, the thermal diffusivity and the Stefan number of the melt. The thermistors arranged within the IDGE thermostat were optimized for measuring the supercooling prior to dendritic growth quite precisely ($\pm$0.002 K). Unfortunately, the subsequent temperature history within the growth chamber, especially during the melting portion of an experimental growth cycle, is less certain. In view of this situation, one can adopt a self-consistent method of estimating the Stefan number in the melt during the last 40 s of the video melting sequence. The basis of the value of the self-consistent Stefan number is the observed extinction time of the fragment, $t^\dagger$. The extinction time (in this instance 40 s) is the interval needed for the melting crystal to disappear. If the left-hand side of Eq. (21) is set equal to zero, a relationship can be established among the Stefan number, the starting size of the crystal $C_0 = 0.76$ cm, and the crystal's extinction time $t^\dagger = 40$ s, namely,

$$St^\dagger = C_0^2/(\alpha_\ell\cdot K_{\text{prol}})\cdot 1/t^\dagger \tag{25}$$

The extinction time can be measured precisely to within one video frame ($\pm$0.033 s), and the thermal diffusivity of molten PVA at its melting point is known to be $\alpha_\ell = 7.0\times10^{-4}$ cm^2/s (Ref. 14). Inserting these values and $K_{\text{prol}} = 360.6$ (see Fig. 5) into Eq. (25) yields the self-consistent Stefan number based on extinction time of $St^\dagger = 0.057$. The crystal melting data reported in Fig. 6 were fit in their entirety using this self-consistent Stefan number, which corresponds to the melt being superheated 0.63 K above its equilibrium melting point $T_m = 35.97$ K. The overall prediction of the melting kinetics throughout the lifetime of this dendrite fragment appears to be in agreement with the quasi-static theory developed in Sec. IV. Scrutiny of the data points shows that there are slight disparities over the melting interval. Particularly as the extinction time is approached, some capillary effects might enter the kinetics and speed

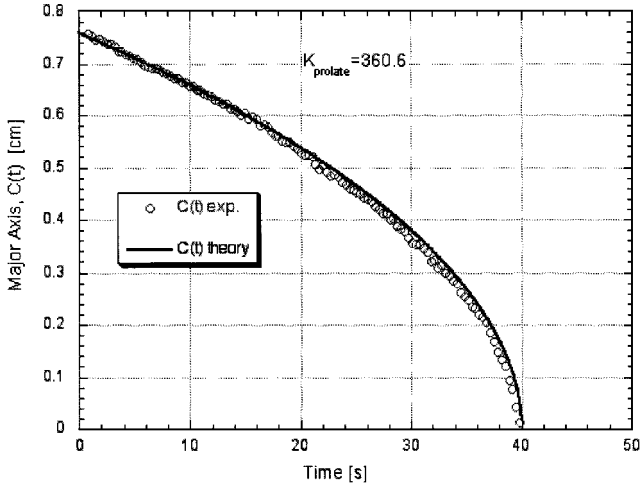

Fig. 6 Melting kinetics of a dendritic PVA crystal fragment ($\mathcal{C}/\mathcal{A}$ = 12) in microgravity. ○, melting data obtained through digital analysis of 30-fps video measured as $\mathcal{C}(t)$ vs time; ——, the theoretical prediction from Eq. (21) fitted with a Stefan number equal to 0.057, corresponding to a temperature rise of 0.63 K above PVA's melting point T_m = 35.97 K.

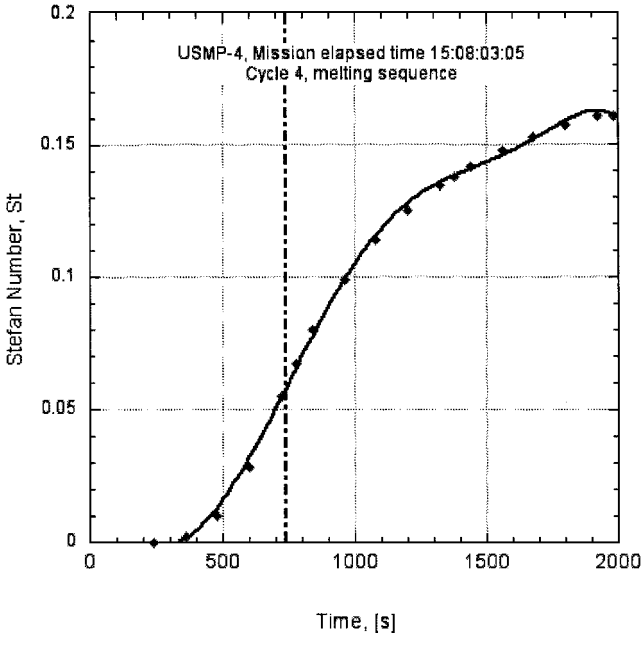

Fig. 7 Melt Stefan number vs time for experimental IDGE cycle with initial supercooling of 0.4 K. The location via direct time synchronization of the dendritic melting interval cannot be placed precisely on the time axis. The completion of the mushy-zone melting process should, however, correspond approximately with the steepest rate of temperature rise within the IDGE growth chamber. The continuous line through the data is based on a sixth-order polynomial, and the vertical line at 720 s marks the steepest rate of Stefan number increase.

up the melting beyond that calculated by quasi-static theory. These are clearly minor effects, and they will be explored in future studies.

Thermal data telemetered from the IDGE thermostat indicate independently that the maximum Stefan number recorded by the high-resolution thermistors internal to the growth chamber at the end of this experimental cycle was about 0.16. See Fig. 7 for these data plotted as Stefan number vs time. Melting of the last dendritic fragments clearly occurred at Stefan numbers much less than 0.16, but the precise range of values over which the observed crystal melted remains imperfectly known, pending closer correlation between the video clock and mission elapsed time. An alternative to obtaining direct thermal measurements is to recognize that the rate of temperature increase in the growth chamber depended on two countervailing factors: 1) the temperature difference between the exterior thermostat temperature (fixed at 37.85°C) and the interior melt temperature and 2) the quantity of crystals within the chamber absorbing latent heat. When melting of the mushy zone begins, the temperature difference is large, approximately 1.8 K, and the chamber contains about 4% crystals. The rate of temperature rise is, however, initially slow, because most of the heat added is absorbed as the latent heat of melting. As the dendrites melt and their mass decreases, the latent heat absorption rate also decreases, and the rate of temperature rise increases. The rate of temperature rise within the IDGE growth chamber should reach its maximum value at about the time at which the last crystals disappear, that is, at the time when our detailed melting data were taken. It is at that point where all latent heat absorption ceases within the chamber, yet the temperature difference between the interior and the exterior is still relatively large (about 1.2 K in this case). We emphasize that this heating rate-time correlation is only approximate. Nonetheless, when the time derivative of the Stefan number vs time is calculated (see Fig. 8), a distinct peak occurs at $t = 720$ s from the start of mushy-zone melting. The time at which the peak rate occurs corresponds to a Stefan number of approximately 0.055. During the 40 s for the melting sequence of the prolate spheroid we selected, the value of the maximum time derivative of the Stefan number is found to be $dSt/dt \cong 2 \times 10^{-4}\ s^{-1}$. Thus, the change of Stefan numbers during the 40-s observation period is ≈0.008. An estimate of the average Stefan number using the IDGE thermal data is 0.055 ± 0.004—in agreement with the self-consistent Stefan number ($St^{\dagger} = 0.057$) determined from Eq. (25) by using the crystal's extinction time.

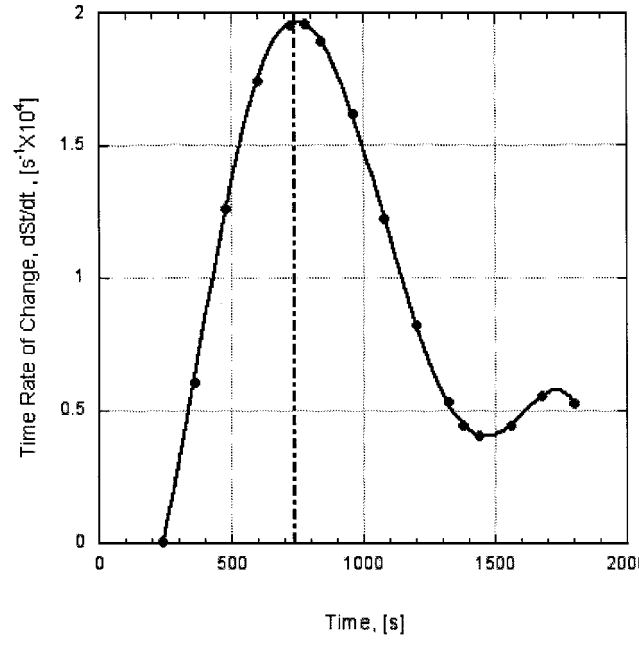

Fig. 8 Time derivative of the melt Stefan number vs time. The continuous curve is based on the derivative of the sixth-order polynomial in Fig. 7. The maximum occurs at 720 s, where the Stefan number is approximately $St \cong 0.055$. See again Fig. 7.

Possible melting behaviors for prolate spheroidal crystals with $\mathcal{C}/\mathcal{A} = 12$, subjected to different Stefan numbers, are shown for comparison in Fig. 9. These curves are predicted using Eq. (21) and the indicated Stefan numbers, which were selected to cover the range of values encountered during the entire melting portion of the experimental cycle. Note that the melting kinetic curves for $\mathcal{C}/\mathcal{A} = 12$ change substantially with only modest variations in the Stefan number. As the aspect ratio of a crystal decreases towards unity, its kinetic melting coefficient rapidly falls toward eight, the limiting value for spheres. Spherical crystals having a diameter $\mathcal{D} = \mathcal{C}$ would exhibit a volume 144 times greater than the prolate spheroid, with an extinction time about 45 times longer than the prolate spheroidal fragment analyzed in Fig. 6. Extinction times for melting are rather sensitive to a crystal's aspect ratio.

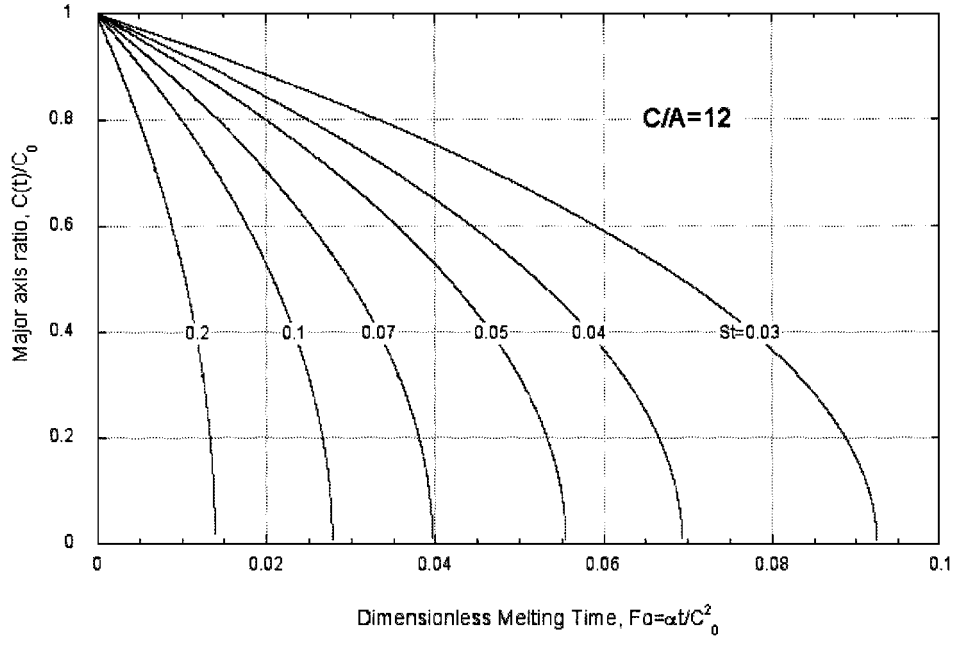

Fig. 9 Major axis length scaled to initial major axis length $\mathcal{C}(t)/\mathcal{C}_0$ vs melting time, predicted by Eq. (21) for $\mathcal{C}/\mathcal{A}$ = 12. These curves show the sensitivity of the melting kinetics for needle-like crystal fragments to the value selected for the Stefan number.

VI. Conclusions

1) Dendritic mushy zones were formed in supercooledhigh-purity PVA melts in microgravity on the third IDGE space flight experiment. At the end of each experimental cycle, the mushy zone was progressively melted by raising the temperature of the thermostat. Video data at 30 fps of the melting process for one cycle (0.4 K supercooling) are reported here. Upon raising the temperature, the mushy zone melts into numerous fragments, many of which can be characterized as prolate spheroids.

2) Individual dendritic fragments remain motionless in the low-gravity environment, progressively melting toward extinction at nearly constant $\mathcal{C}/\mathcal{A}$ ratios.

3) Moving boundary solutions, such as those proposed by Ham for ellipsoidal crystals, are not applicable to melting processes. In lieu of a numerical solution to the moving boundary problem, we developed a quasi-static analytic theory, using curvilinear coordinates. The theory describes the kinetics of conduction melting of prolate spheroids of arbitrary $\mathcal{C}/\mathcal{A}$ ratios. The quasi-static analytic results are limited to small Stefan numbers ($St \ll 1$).

4) The observed melting kinetics in microgravity of a prolate spheroidal crystal with an aspect ratio $\mathcal{C}/\mathcal{A} = 12$ was found to be described accurately by the quasi-static analysis. Predictions of the crystal size as a function of time require knowledge of the Stefan number, the melt's thermal diffusivity, and a kinetic parameter derived from the theory that accounts for the crystal's aspect ratio.

5) The Stefan number for this work was found from the extinction time of the crystal. Temperature data telemetered directly from the orbiting IDGE thermostat yield a Stefan number in good agreement with the value derived from the extinction time of the prolate spheroid analyzed. The predicted convection-free melting kinetics accurately describe the experimental observations in microgravity.

6) Future work will be directed at obtaining a direct precision measurement of the Stefan numbers using in situ thermometry and exploring the influences of the initial supercooling that affect mushy zone morphology and density. In addition, small disparities discovered between the microgravity melting data and quasi-static theory, perhaps caused by ignoring capillary effects, will be the subject of future enquiry.

Acknowledgments

The authors gratefully acknowledge the support provided for this work by NASA, Division of Biological and Physical Sciences Research, Code U, Washington, DC, under Grant NAG 8-1696. Special thanks are given to Diane Malarik, IDGE Project Manager, NASA Glenn Research Center, Cleveland, OH, who provided USMP-4 mission data which assisted our efforts.

References

[1]Glicksman, M. E., and Marsh, S. P., "The Dendrite," *Handbook of Crystal Growth*, edited by D. T. J. Hurle, Elsevier, Amsterdam, 1993, pp. 1075–1122.

[2]Langer, J. S., and Muller-Krumbhaar, H., "Theory of Dendritic Growth. I. Elements of a Stability Analysis," *Acta Metallurgica*, Vol. 26, No. 1, 1978, pp. 1681–1687.

[3]Langer, J. S., "Non-equilibrium Physics and the Origins of Complexity in Nature," *Princeton Series in Physics: Critical Problems in Physics*, Princeton Univ. Press, Princeton, NJ, 1996, Chap. 2.

[4]Mullins, W. W., and Sekerka, R. F., "Morphological Stability of a Particle Growing by Diffusion of Heat Flow," *Journal of Applied Physics*, Vol. 34, No. 2, 1963, pp. 323–329.

[5]Kessler, D., and Levine, H., "Velocity Selection in Dendritic Growth," *Physical Review B*, Vol. 33, No. 11, 1986, pp. 7867–7870.

[6]Glicksman, M. E., Schaefer, R. J., and Ayers, J. D., "Dendritic Growth—A Test of Theory," *Metallurgical Transactions A*, Vol. 7A, No. 1, 1976, pp. 1747–1759.

[7]Glicksman, M. E., "Fundamentals of Dendritic Crystal Growth," *Crystal Growth of Electronic Materials*, edited by E. Kaldis, Elsevier, Amsterdam, 1985, Chap. 5, pp. 57–69.

[8]Huang, S. C., and Glicksman, M. E., "Fundamentals of Dendritic Solidification—I. Steady-State Tip Growth," *Acta Metallurgica*, Vol. 29, No. 5, 1981, pp. 701–715.

[9]Trivedi, R., and Mason, J. T., "The Effects of Interface Attachment Kinetics on Solidification Interface Morphologies," *Metallurgical Transactions A*, Vol. 22A, No. 1, 1991, pp. 235–249.

[10]Lipton, J., Glicksman, M. E., and Kurz, W., "Equiaxed Dendrite Growth in Alloys at Small Supercooling," *Metallurgical Transactions A*, Vol. 18A, No. 2, 1987, pp. 341–345.

[11]Glicksman, M. E., Koss, M. B., Bushnell, L. T., Lacombe, J. C., and Winsa, E. A., "The Isothermal Dendritic Growth Experiment," *Materials Science Forum*, Vols. 215–216, No. 2, 1996, pp. 179–190.

[12]LaCombe, J. C., Koss, M. B., Fradkov, V. E., and Glicksman, M. E., "Three-Dimensional Dendrite-Tip Morphology," *Physical Review, E*, Vol. 52, No. 3, 1995, pp. 2778–2786.

[13]LaCombe, J. C., Koss, M. B., Corrigan, D. C., Lupulescu, A., and Tennenhouse, L. A., "Implications of the Interface Shape on Steady-State Dendritic Crystal Growth," *Journal of Crystal Growth*, Vol. 206, No. 4, 1999, pp. 331–344.

[14]Lupulescu, A., LaCombe, J. C., Frei, J. E., Glicksman, M. E., and Koss, M. B., "USMP-4 Microgravity PVA Dendritic Growth Data—Preliminary Analysis," *Microgravity Symposium: Proceedings TMS Meeting* [CD-ROM], Minerals, Metals, and Materials Society, Warrendale, PA, 2000.

[15]Ivantsov, G. P., "The Temperature Field Around Spherical, Cylindrical, and Needle-Shaped Crystals Which Grow in Supercooled Melts," *Doklody Akademii Nauk USSR*, Vol. 58, No. 4, 1947, pp. 567–569.

[16]Marsh, S. P., and Glicksman, M. E., "Overview of Geometric Effects on Coarsening of Mushy Zones," *Metallurgical and Materials Transactions A*, Vol. 27A, No. 3, 1996, pp. 557–567.

[17]Paradies, C. J., Smith, R. N., and Glicksman, M. E., "The Influence of Convection During Solidification on Fragmentation of the Mushy Zone of a Model Alloy," *Metallurgical and Materials Transactions A*, Vol. 28A, No. 3A, 1997, pp. 875–883.

[18]Fearn, D. R., Loper, D. E., and Roberts, P. H., "Structure of the Earth's Inner Core," *Nature*, Vol. 292, No. 5820, 1981, pp. 232, 233.

[19]Loper, D. E., "Structure of the Inner Core Boundary," *Geophysical, Astrophysical, Fluid Dynamics*, Vol. 25, Nos. 1–2, 1983, pp. 139–155.

[20]Wenk, H. R., Takeshita, T., Jeanloz, R., and Johnson, G. C., "Development of Texture and Elastic Anisotropy During Deformation of hcp Metals," *Geophysical Research Letters*, Vol. 15, No. 1, 1988, pp. 76–79.

[21]Cormier, V. F., "Inner Core Structure Inferred from Body Waveforms," *EOS*, Vol. 75, 1994, p. 67.

[22]Souriau, A., and Romanowicz, B., "Anisotropy in Inner Core Attenuation: A New Type of Data to Constrain the Nature of the Solid Core," *Geophysical Research Letters*, Vol. 23, No. 1, 1996, pp. 1–4.

[23]Bergman, M. I., "Measurements of Elastic Anisotropy Due to Solidification Texturing and the Implications for the Earth's Inner Core," *Nature*, Vol. 389, No. 6646, 1997, pp. 60–63.

[24]Rushmer, T., Minarik, W. G., and Taylor, G. J., "Physical Processes of Core Formation," *Origin of the Earth and Moon*, edited by R. M. Canup and K. Righter, Univ. of Arizona Press, Tucson, AZ, 2000, pp. 227–245.

[25]Haack, H., and Scott, E. R. D., "Asteroid Core Crystallization by Inward Dendritic Growth," *Journal of Geophysical Research*, Vol. 97, No. E9, 1992, pp. 14,727–14,734.

[26]Esbensen, K. H., and Buchwald, V. F., "Planet(oid) Core Crystallization and Fractionation—Evidence from the Agpalilik Mass of the Cape York Iron Meteorite Shower," *Physics of the Earth and Planetary Interiors*, Vol. 29, Nos. 3–4, 1982, pp. 218–232.

[27]Sekerka, R. F., Jeanfils, C. L., and Heckel, R. W., "The Moving Boundary Problem," *Lectures on the Theory of Phase Transformations*, edited by H. I. Aaronson, Metallurgical Society, New York, 1982, pp. 117–169.

[28]Glicksman, M. E., *Diffusion in Solids: Field Theory, Solid-State Principles, and Applications*, Wiley, New York, 2000.

[29]Ham, F. S., "Shape-Preserving Solutions of the Time-Dependent Diffusion Equation," *Quarterly Journal of Applied Mathematics*, Vol. 17, 1959, pp. 137–145.

[30]Horvay, G., and Cahn, J. W., "Dendritic and Spheroidal Growth," *Acta Metallurgica*, Vol. 9, No. 7, 1961, pp. 695–705.

[31]Andreucci, D., Herrero, M. A., and Velasquez, J. J. L., "The Classical One-Phase Stefan Problem: A Catalog of Interface Behaviors," *Surveys on Mathematics for Industry*, Vol. 9, pp. 273–281.

[32]Morse, P. M., and Feshbach, H., *Methods of Theoretical Physics*, Vol. 2, McGraw–Hill, New York, 1953, pp. 1284–1292.

[33]Eshbach, O. W., *Handbook of Engineering Fundamentals*, 2nd ed., Wiley, New York, 1961, pp. 2–60.

[34]McFadden, G. B., and Coriell, S. R., "The Effect of Fluid Flow Due to the Crystal-Melt Density Change on the Growth of a Parabolic Isothermal Dendrite," *Journal of Crystal Growth*, Vol. 74, No. 3, 1986, pp. 507–512.

[35]Karma, A., and Plapp, M., "Phase-Field Modeling of Coupled Growth in Binary and Ternary Alloys," AIAA Reprint 2002-0600, Jan. 2002.